Chemistry, Physics and Technology of Surface. 2022. V. 13. N 4. P. 361-382

PACS: 61.05.C−; 61.43.Gt; 68.37.Og; 68.43.-h; 68.47.Gh doi: 10.15407/hftp13.04.361

V.M. Gun'ko

MORPHOLOGIC AND TEXTURAL EFFECTS OF GELATION AND MECHANOCHEMICAL ACTIVATION ON DRY OR WETTED SIMPLE AND COMPLEX NANOOXIDES

Chuiko Institute of Surface Chemistry of National Academy of Sciences of Ukraine
17 General Naumov Str., Kyiv, 03164, Ukraine, E-mail: vlad_gunko@ukr.net

The characteristics and properties of fumed oxides depend strongly on various external actions that is of importance from a practical point of view. Therefore, gelation or high-pressure cryogelation (HPC) of aqueous media pure or with 0.1 M NaCl, and mechanochemical activation (MCA) of dry or wetted powders of individual (silica, alumina, their mechanical blends) and complex (silica/titania, alumina/silica/titania, AST1, AST1/A–300) nanooxides were studied to analyze the influence of the nanooxide composition, particulate morphology, and preparation conditions on changes in the morphological and textural characteristics of treated samples. The temperature–pressure behavior of different phases (silica, alumina, and titania) under HPC can result in destroy of complex core-shell nanoparticles (100–200 nm in size) in contrast to small nonporous nanoparticles, NPNP (5–20 nm). The textural characteristics of nanooxides are sensitive to any external actions due to compaction of such supra-NPNP structures as aggregates of nanoparticles, agglomerates of aggregates, and visible structures in powders. The compaction of supra-NPNP enhances the pore volume but much weakly affects the specific surface area (with one exception of AST1) because small NPNP are relatively stable during any external actions (HPC, MCA). The compacted materials are characterized by enhanced mesoporosity shifted to macroporosity with decreasing specific surface area and increasing sizes of nanoparticles or to mesopores with increasing MCA time or amounts of water in wetted powders. At low hydration of the A–300 powder (h = 0.5 g/g), the value of S_{BET} slightly increases if MCA is provided by stirring or ball-milling. Diminution of the freezing temperature from 208 to 77.4 K during HPC results in enhanced compaction of aggregates and agglomerates but this does not practically affect the primary nanoparticles. The degree of decomposition of core-shell nanoparticles of AST1 does not practically increase with decreasing freezing temperature from 208 to 77.4 K. Decomposition of core-shell AST1 particles is inhibited under HPC by added A–300 (1 : 1) working as a damper.

Keywords: *nanosilica, nanoalumina, silica/titania, alumina/silica/titania, high-pressure cryogelation, morphological and textural characteristics*

INTRODUCTION

The formation and distribution of various phases in nonporous nanoparticles (NPNP) of binary and ternary fumed oxides depend not only on the content of reactants (*e.g.*, MCl_n, where M = Al, Si, and Ti, n = 3 or 4) in the O_2/H_2 flame but also on certain differences in the reactivity (in the flame) of precursors [1–6]. For example, $AlCl_3$ forming solid Al_2Cl_6 should be sublimated, its melting point is relatively high (180 °C), and vapor pressure is relatively low (*e.g.*, 13.3 kPa at 151 °C). $SiCl_4$ is liquid at low boiling point (57.65 °C), and vapor pressure is relatively high (25.9 kPa at 20 °C). $TiCl_4$ is liquid at higher boiling point (136.4 °C) and at lower vapor pressure (1.3 kPa at 20 °C). The distribution of precursors in the flame, flame turbulence, length, and temperature gradient also affect the NPNP structure formed at high temperatures [1–16]. In other words, there are many factors strongly governing the structure of NPNP of complex fumed metal or metalloid oxides (CFMO) that lead to significant nonuniformity of the NPNP interior and surface, especially for SA and AST1, as well as to changes in the particle size distributions (PaSD) [16, 17]. For CFMO, there are several possible NPNP structures with: (i) practically individual phase, (ii) solid solution of one phase in another, (iii) simple core-shell, (iv) simple or complex shell – polycrystalline or amorphous core, and (v) complex shell – complex core [16, 17]. The flame synthesis of fumed oxides at high temperatures corresponds to relatively fast nonequilibrium processes of the NPNP formation occurring during a fraction of a second. This results in significant amorphism and nonuniformity of CFMO NPNP. NPNP form agglomerates (< 1 μm) and agglomerates of

aggregates (> 1 μm) forming visible loose particles of the CFMO powders. All these hierarchical structures could be attributed to supra-NPNP. The bulk density (ρ_b) of fumed oxide powders could be low as 0.04–0.05 g/cm^3. This corresponds to large empty volume $V_{em} = 1/\rho_b - 1/\rho_0$ (ρ_0 is the true density of NPNP) up to 25 cm^3/g for fumed silica. It could be smaller for CFMO due to larger ρ_b and ρ_0 values and NPNP sizes. Despite these values are larger than that of nanosilica, the CFMO powders are quite loose [1–7, 16, 17]. Fumed silica alone or in CFMO is always amorphous [1–6, 16, 17]. Alumina and titania in CFMO could form both amorphous and crystalline phases, *e.g.*, γ-, δ-, θ-, and α-Al_2O_3 of increased stability with increasing heating temperature, respectively, and titania with anatase or/and rutile [17]. The phase composition of CFMO NPNP (as well as of other oxides) depends on the synthesis temperature, reciprocal effects of components, and other synthesis conditions [17–26]. For example, silica stabilizes anatase and inhibits the formation of rutile in fumed titania/silica, but a small amount of alumina can cause the formation of rutile, and these effects depend on the flame temperature [16, 17, 21, 22].

One of important structural features of fumed nanooxides is the absence of valence bonding of primary nanoparticles in their aggregates and agglomerates of aggregates [1–6, 27–29]. This bonding is mainly due to electrostatic and dispersion forces and hydrogen bonds between surface hydroxyls of adjacent nanoparticles. Adsorbed water located in contact zones of adjacent nanoparticles can play a certain role in this bonding [16]. The nanooxide powders are rather "soft" matters of a low bulk density and a small amount of water (0.5–3 wt. % for nanosilicas) adsorbed from air. Some treatments (such as hydrothermal, thermal, chemical modification of a surface with cross-linking of modifiers, *etc.*) of nanooxides can lead to formation of chemical bonds between adjacent nanoparticles. Surface hydroxyls play an important role in this bonding, as well as in many other properties of nanooxides. Another problem related to changes in the morphology of nanoparticles *per se* during different treatments is less studied than effects of surface modification of nanoparticles. Notice that nanooxides can be used in the form of aqueous suspensions pure or with 0.1 M NaCl as medicinal preparations [30]. Therefore, the NaCl effects on the behavior of nanooxides in initial and frozen suspensions are of interest for practical applications. For example, pure aqueous suspensions of nanosilica frozen and then thawed lose the aggregative stability and cannot be completely re-suspended.

Previously [31–33], high-pressure cryogelation (HPC) of nanooxides was studied using concentrated aqueous suspensions (5–20 wt. %) at low temperature (77–260 K) and high pressures (450–1000 atm) in comparison with the initial powder and suspended-dried samples prepared under standard conditions. During HPC, ice crystallites playing a role of porogens [34] can produce very high pressure in restricted volume (up to 2000 atm in a container with absolutely rigid walls and ~1050 atm in a freezing bomb with stainless steel) [35]. Obtained results [31–33] showed changes in the textural and adsorption characteristics of nanooxides dependent on its concentration in the suspensions and HPC conditions. Composition of nanoparticles of complex oxides affects results of HPC and the properties of final cryogels due to the differences in the pressure and temperature behavior of different phases in complex nanoparticles.

Cryogels with inorganic materials (including silica, alumina, titania, *etc.*), as well as gels, can be synthesized using low-molecular weight compounds (*e.g.,* tetraethyl orthosilicate, titanium tetraisopropoxide, metal chlorides, *etc.*) or high-molecular weight compounds [34, 36–57]. Oxide nanoparticles can be considered as analogues of polymers used in cryogelation with cross-linking of macromolecules [34]. The textural and morphological characteristics of inorganic cryogels can be varied depending on water content (since ice crystallites play a role of a porogen templating pores), precursor types, time, temperature, temperature gradient, and other conditions [36–57]. During preparation, some inorganic cryogels were frozen at very low temperatures (77.4 K) [36–38]. However, higher temperatures (between −12 and −20 °C) are typically used in cryogelation. Despite numerous papers published on inorganic gels and cryogels (see, *e.g.* [31–57] and references therein), there is a small number of publications on cryogels with complex nanooxides prepared at low temperatures and high pressures (~1000 atm) in cryo-bombs.

Silica cryogels can have the structural and textural characteristics close to those of silica aerogels that is of importance from practical point of view since cryogelation is a simpler and faster method than aerogelation. High pressure cryogelation is an additional pathway to synthesize cryogels with the characteristics controlled with respect to both macropores and narrow pores, since high pressures (*e.g.*, at 450–1000 atm in cryo-bombs with stainless steel) can change the structure of particles, pores, and macropore walls, as well as other characteristics [17, 31–33]. HPC can be used with the imprinting technique to modify a surface of cryogels. In contrast to aerogel synthesis with a high-pressure drying stage in the CO_2 atmosphere replacing a solvent medium, HPC uses the natural pressure effect caused by transformation of water into ice with increased volume. To remain high pressure produced by ice, freezing bombs with restricted volume within strongly rigid walls could be used [31–35]. During cryogelation, the supra-NPNP structures of nanooxides can be easily changed. Changes in the morphology of nanoparticles (especially composed with one matter) are less probable during HPC because these nanoparticles are nonporous, therefore ice crystallites cannot provide disjoining pressure inside nanoparticles. However, the temperature–pressure behavior of nanoparticles of binary and ternary nanooxides of larger sizes can be more complex in HPC [31–33]. For instance, there is a certain difference in the behavior of crystalline (*e.g.*, alumina, titania) and amorphous (silica) nanoparticles, especially relatively large (100–200 nm in size) core–shell nanoparticles, during HPC [31–33]. Fumed core–shell particles can be destroyed during HPC (since the *S* value strongly increases after HPC) in contrast to small primary nanoparticles composed with one matter and characterized by the *S* value remaining practically the same after HPC [31–33].

Thus, "soft" hierarchical structure (*i.e.*, supra-NPNP) of nanooxides is sensitive to any external actions such as pressing, mechanochemical activation (MCA), gelation (hydro-compaction), cryogelation, *etc*.; however, NPNP are typically more stable [16, 17, 19–26, 31–33]. These aspects are of interest from practical point of view. Therefore, the aim of this work was to generalize information on the effects of chemical composition of nanooxides (different amounts of components in compositions with silica/alumina, silica/titania, and alumina/silica/titania) and gelation conditions (temperature, pressure, water amounts, post-HPC treatment) in comparison to dried gels prepared under standard conditions without freezing or initial powders after MCA on the morphological and textural characteristics of nanooxides.

MATERIALS AND METHODS

Individual oxides: fumed nanosilica A–300 (several samples) and fumed nanoalumina (S_{BET} = 89 m^2/g), binary fumed silica/titania ST63, ST80 and ST94 (63, 80, and 94 wt. % of titania, respectively), titania/silica at 20 wt. % of titania synthesized using A–100 (S_{BET} ≈ 100 m^2/g) as a substrate by chemical vapor deposition (CVD) method (label CVD–ST20), and fumed alumina/silica/titania, AST1 (89 wt. % of partially crystalline alumina, 10 wt. % of amorphous silica, and 1 wt. % of titania as a small number of titania nanoparticles doped by silica and alumina and a solid solution of titania in alumina and silica phases, S_{BET} = 83 m^2/g) were used as the initial powder materials (Pilot plant of the Chuiko Institute of Surface Chemistry, Kalush, Ukraine). Some powders (preheated at 723 K for 2 h) were mechanochemically activated in a stainless steel microgrinder (30 W, volume 10 cm^3 with a stainless-steel ball of 0.8 cm in diameter) for 5 or 30 min or in a ball-mill for 1–24 h (dry or wetted powders).

Aqueous suspensions of nanooxides (5, 10, 15, or 20 wt. %) were prepared using doubly distilled water (pure or with 0.1 M NaCl, dried samples labels cs or gs) by sonication (22 kHz) for 5 min. The dispersions were then frozen at 260 K (for 12 or 24 h) or 208 K (for 12 h) or 260 K (for 24 h) and them 77.4 K (for 4 h) or 77.4 K (4 h) in thick-walled stainless-steel reactors at pressures of up to 1050 atm, caused by ice crystallites formed in the frozen suspensions (~10–15 mL) placed in strongly restricted volume of the cryo-bombs. Then cryonanooxide samples were dried in glass dishes in air at room temperature for 2–5 days to air-dry state (label cryogels, c). The same suspensions prepared at standard conditions were kept at room temperature for 24 h and 1 atm to prepare gelled samples (label gel, g) and then dried for 2–5 days to air-dry state. All the final materials studied were prepared in the powder state.

To analyze the textural characteristics of initial and differently treated nanooxides degassed at 373 K for several hours (Table 1), low-temperature (77.4 K) nitrogen adsorption–desorption isotherms

were recorded using a Micromeritics ASAP 2420 (V2.09 J) adsorption analyzer. The specific surface area (S_{BET}, Tables 1–4) was calculated according to the standard BET method [58]. The total pore volume (V_p) was evaluated from the nitrogen adsorption at $p/p_0 \approx 0.99$, where p and p_0 denote the equilibrium and saturation pressure of nitrogen at 77.4 K, respectively. The nitrogen desorption data were used to compute the pore size distributions (PSD, differential $f_V(R) \sim dV_p/dR$ and $f_S(R) \sim dS/dR$) with the density functional theory (DFT) method [59, 60] using a self-consistent regularization (SCR) procedure under non-negativity condition ($f_V(R) \geq 0$ at any pore radius R) at a fixed regularization parameter $\alpha = 0.01$ with a complex pore model with cylindrical (C) pores and voids (V) between spherical nonporous nanoparticles packed in random aggregates. The void-cylindrical pore model was used for one (CV/SCR) or two (VCV/SCR) materials such as silica and titania or alumina and silica using the parameters for these materials [59, 60]. In the case of VCV/SCR, two different nanoparticle size distributions are used upon the DFT calculations because A–300 and nanoalumina or AST1 are composed of particles with different PaSD [16, 17] that reflects in different values of S_{BET}. Two shapes (VC) of pores are used for a major phase, and single shape (V) of pores is used for a minor phase. The differential PSDs with respect to pore volume $f_V(R) \sim dV/dR$, $\int f_V(R)dR \sim V_p$ were re-calculated to incremental PSD (IPSD) at $\Phi_V(R_i) = (f_V(R_{i+1}) + f_V(R_i))(R_{i+1}-R_i)/2$ at $\sum\Phi_V(R_i) = V_p$). The differential $f_S(R)$ functions were used to estimate the deviation of the pore shape from the model as follows

$$\Delta w = \left(S_{BET} / \int_{R_{min}}^{R_{max}} f_S(R)dR \right) - 1, \quad (1)$$

where R_{max} and R_{min} are the maximal and minimal pore radii, respectively [61]. The $f_V(R)$ and $f_S(R)$ functions were also used to calculate contributions of nanopores (V_{nano} and S_{nano} at 0.35 nm < R < 1 nm), mesopores (V_{meso} and S_{meso} at 1 nm < R < 25 nm), and macropores (V_{macro} and S_{macro} at 25 nm < R < 100 nm). The average values of the pore radii were determined with respect to both pore volume and specific surface area, respectively, as the corresponding moments of the distribution functions

$$< R_V >= \int_{R_{min}}^{R_{max}} Rf_V(R)dR / \int_{R_{min}}^{R_{max}} f_V(R)dR, \quad (2)$$

$$< R_S >= \int_{R_{min}}^{R_{max}} Rf_S(R)dR / \int_{R_{min}}^{R_{max}} f_S(R)dR. \quad (3)$$

Additionally, the PSD were calculated using nonlocal density functional theory (NLDFT) method [62] using equilibrium model of cylindrical pores in silica.

High resolution transmission electron microscopy, HRTEM (JEM–2100F, Japan) images were recorded for initial A–300, cryosilica cA–300, initial AST1, and cryonanooxide cAST1 as representative samples. A powder sample was added to acetone (for chromatography) and sonicated. Then a drop of the suspension was deposited onto a copper grid with a thin carbon film. After acetone evaporation, sample particles remained on the film were studied with HRTEM.

X-ray diffraction (XRD) patterns of samples were recorded over 2θ = 10–80° range using DRON–4–07 (Burevestnik, St. Petersburg) and Ultima IV (Rigaku, Japan) diffractometers with CuK_α (λ = 0.15418 nm) radiation and a Ni filter. Analysis of the crystalline structure was carried out using the JCPDS Database (International Center for Diffraction Data, PA, 2001) [63].

RESULTS AND DISCUSSION

Different levels of the structural hierarchy: NPNP (Figs. 1–5) → NPNP aggregates → agglomerates of aggregates → visible particles of fumed oxides are characterized by a different degree of the strength and rigidity. Typically, the smaller the structures the greater their strength and rigidity appearing under various external actions studied here. As a whole, supra-NPNP structures are much softer than individual NPNP, and larger core-shell NPNP (100–200 nm, Fig. 4) are less stable than smaller simple NPNP (5–20 nm, Figs. 1–5) during MCA or HPC (Tables 1–4). These features are weakly affected by the crystallinity and amorphism of NPNP (Figs. 1–7). However, various external actions (such as pressing, wetting-drying-heating, MCA of dry and wetted powders or suspensions, gelation, cryogelation, and HPC) on simple and complex nanooxides and their blends can change not only supra-NPNP structures (*i.e.*, textural characteristics, Tables 1–4, Figs. 8–13) but also

Table 1. Textural characteristics of initial powders and treated and dried suspensions (20 wt. %) of silica A–300 (DFT CV/SCR method)

Sample	T, K	P, atm	S_{BET}, m^2/g	S_{nano}, m^2/g	S_{meso}, m^2/g	S_{macro}, m^2/g	V_p, cm^3/g	V_{nano}, cm^3/g	V_{meso}, cm^3/g	V_{macro}, cm^3/g	$\langle R_V \rangle$, nm	$\langle R_S \rangle$, nm	a, nm	Δw
Initial			303	180	109	14	0.735	0.065	0.423	0.247	23.6	5.3	4.5	0.167
Gel	293[a]	1	292	88	204	0	1.198	0.032	1.165	0.001	14.0	8.6	4.7	0.114
Gel/NaCl	293[a]	1	264	69	195	0	1.258	0.029	1.228	0	13.3	8.7	5.2	-0.036
Gel/NaCl washed	293[a]	1	276	73	203	0	1.313	0.029	1.283	0	13.9	9.1	4.9	0.009
Cryogel	208[a]	1000	297	87	210	0.1	1.384	0.032	1.350	0.001	15.2	9.5	4.6	0.085
Cryogel/NaCl	260[b]	1000	262	67	195	0	1.195	0.028	1.166	0	12.3	8.3	5.2	-0.034
Cryogel/NaCl washed	260[b]	1000	279	72	207	0	1.291	0.030	1.261	0	12.7	8.6	4.9	-0.021
Cryogel/NaCl	208[a]	1000	282	81	201	0	1.246	0.031	1.214	0.001	14.1	8.8	4.8	0.053
Cryogel/NaCl(rep)	208[a]	1000	282	80	202	0	1.212	0.032	1.178	0.002	13.5	8.3	4.8	0.027
Initial			323	161	142	20	0.790	0.046	0.470	0.274	22.7	6.5	4.2	0.413
MCA 1 h (dry)			301	86	183	32	1.591	0.031	1.035	0.525	22.4	11.1	4.5	0.115
MCA 2 h (dry)			305	91	192	22	1.399	0.033	0.995	0.372	20.5	9.7	4.5	0.117
MCA 4 h (dry)			301	97	193	11	1.110	0.035	0.875	0.199	17.0	7.6	4.5	0.092
MCA 8 h (dry)			293	104	182	7	0.862	0.039	0.688	0.135	15.3	5.9	4.7	0.059
MCA 12 h (dry)			282	102	174	6	0.766	0.039	0.613	0.115	14.6	5.4	4.8	0.049
MCA 18 h (dry)			273	105	163	5	0.680	0.040	0.540	0.100	13.8	4.9	5.0	0.036
MCA 24 h (dry)			257	95	157	5	0.652	0.038	0.514	0.100	14.1	4.8	5.3	0.004
Initial			330	121	190	19	0.826	0.026	0.493	0.307	28.3	7.6	4.1	0.342
MCA 1 h (wetted, h = 0.5 g/g)			345	109	204	32	1.419	0.033	0.888	0.498	23.2	9.8	4.0	0.071
MCA 6 h (wetted, h = 0.5 g/g)			332	108	223	0.9	0.771	0.044	0.691	0.037	9.0	4.1	4.1	-0.021

Note. [a]Gelation for 12 h and [b]24 h; a is the average radius NPNP

Table 2. Textural characteristics of initial powders and treated suspensions dried of silica, alumina and silica/alumina blends (DFT VCV/SCR method)

Sample	T, K	C_{ox}, wt. %	P, atm	S_{BET}, m^2/g	S_{nano}, m^2/g	S_{meso}, m^2/g	S_{macro}, m^2/g	V_p, cm^3/g	V_{nano}, cm^3/g	V_{meso}, cm^3/g	V_{macro}, cm^3/g	$\langle R_V \rangle$, nm	$\langle R_S \rangle$, nm	a, nm
A–300				330	134	178	18	0.826	0.032	0.517	0.277	25.5	7.3	4.1
Al_2O_3				89	27	56	6	0.167	0.004	0.098	0.065	27.6	7.2	8.4
cA–300	208	5	1000	280	89	190	1	1.474	0.035	1.422	0.018	16.1	10.1	4.9
cA–300	208	10	1000	293	89	203	0	1.341	0.036	1.305	0	12.7	8.4	4.7
cA–300	208	20	1000	289	91	198	0	1.298	0.038	1.260	0	12.0	8.0	4.7
gAl_2O_3	293	20	1	76	11	64	1	0.545	0.003	0.525	0.016	18.4	14.4	9.9
gsAl_2O_3[a]	293	20	1	72	13	39	21	0.521	0.004	0.224	0.294	28.0	17.2	10.4
csAl_2O_3[a]	208	20	1000	72	12	41	20	0.553	0.004	0.258	0.292	26.7	17.2	10.4
A–300/Al_2O_3(1:1)				165	0	142	23	0.541	0	0.281	0.259	31.0	13.4	5.9
A–300/Al_2O_3(1:3)				116	0	97	19	0.434	0	0.211	0.224	34.6	15.3	7.3
A–300/Al_2O_3(3:1)				226	0	197	29	0.670	0	0.363	0.307	30.0	12.7	5.0
gA–300/Al_2O_3(1:1)	293	5	1	173	0	150	23	0.543	0	0.291	0.252	30.9	13.3	5.6
gA–300/Al_2O_3(1:3)	293	5	1	119	0	101	18	0.426	0	0.219	0.207	33.2	14.9	7.1
gA–300/Al_2O_3(3:1)	293	5	1	231	0	202	29	0.678	0	0.378	0.300	29.2	12.5	4.9
cA–300/Al_2O_3(1:1)	208	5	1000	171	0	147	24	0.549	0	0.289	0.260	31.7	13.7	5.7
cA–300/Al_2O_3(1:3)	208	5	1000	115	0	98	17	0.426	0	0.215	0.211	33.6	15.1	7.4
cA–300/Al_2O_3(3:1)	208	5	1000	227	0	198	29	0.682	0	0.376	0.307	29.5	12.7	5.0
cA–300/Al_2O_3(1:1)[h]	208	5	1000	164	0	142	22	0.541	0	0.279	0.261	35.1	14.4	5.9
cA–300/Al_2O_3(1:3)[h]	208	5	1000	111	0	92	19	0.424	0	0.213	0.211	32.8	15.3	7.6
cA–300/Al_2O_3(3:1)[h]	208	5	1000	218	0	187	31	0.706	0	0.367	0.339	32.5	14.1	5.2

Note. [a] The suspensions with 0.1 M NaCl; dried at room temperature and [h]heated at 873 K. The values of V_{nano} and S_{nano}, V_{meso} and S_{meso}, and V_{macro} and S_{macro} were calculated by integration of the $f_V(R)$ and $f_S(R)$ functions at 0.35 nm < R < 1 nm, 1 nm < R < 25 nm, 25 nm < R < 100 nm, respectively

Table 3. Textural characteristics of initial powders and treated aqueous suspensions dried of AST1 silica/AST1 blends (DFT VCV/SCR method)

Sample	T, K	C_{ox}, wt. %	P, atm	S_{BET}, m^2/g	S_{nano}, m^2/g	S_{meso}, m^2/g	S_{macro}, m^2/g	V_p, cm^3/g	V_{nano}, cm^3/g	V_{meso}, cm^3/g	V_{macro}, cm^3/g	$<R_V>$, nm	$<R_S>$, nm	a, nm
AST1				83	30	46	7	0.217	0.006	0.116	0.096	27.8	8.5	9.5
gAST1	293	20	1	74	11	45	18	0.532	0.003	0.280	0.249	25.3	16.4	10.6
cAST1	208	20	1000	160	33	116	11	0.595	0.007	0.459	0.129	19.9	10.4	4.9
gsAST1	293	20[a]	1	120	26	76	18	0.506	0.006	0.252	0.248	28.4	12.0	6.6
csAST1	208	20[a]	1000	133	30	84	19	0.508	0.006	0.264	0.238	26.5	11.1	5.9
cAST1	260/77.4	20	1000	158	29	127	2	0.598	0.008	0.553	0.037	15.0	8.5	5.0
cAST1	77.4	20	1000	160	32	125	3	0.571	0.008	0.507	0.056	16.5	8.7	4.9
gA–300/AST1(1:1)	293	20	1	147	0	71	76	1.029	0	0.221	0.808	39.5	26.6	6.8
cA–300/AST1(1:1)	208	20	1000	147	0	72	75	1.098	0	0.246	0.852	37.3	26.8	6.8
gsA–300/AST1(1:1)	293	20[a]	1	155	0	78	77	1.064	0	0.252	0.812	36.9	26.1	6.4
csA–300/AST1(1:1)	208	20[a]	1000	155	0	69	86	1.142	0	0.248	0.894	35.9	27.5	6.4

Note. Gelation of all samples was during 12 h. The first symbols in labels of dried samples correspond to cryogel (c), cryogel with salt NaCl (cs), [a] the suspensions with 0.1M NaCl dried at room temperature, gelation at 293 K for 12 h (g) with NaCl (gs)

Table 4. Textural characteristics of initial and differently treated nanooxides (DFT VCV/SCR method). The differential $f_S(R)$ functions were used to estimate the deviation of the pore shape from the model as follows

Oxide	T_t, K	P_t, atm	State	S_{BET}, m^2/g	S_{nano}, m^2/g	S_{meso}, m^2/g	S_{macro}, m^2/g	V_p, cm^3/g	V_{nano}, cm^3/g	V_{meso}, cm^3/g	V_{macro}, cm^3/g	$<R_V>$, nm	$<R_S>$, nm	a, nm
CVDST20	–	–	Initial powder	64	27	30	7	0.165	0.005	0.067	0.094	36.8	8.5	18.2
gCVDST20	298	1	Gel	65	22	32	10	0.236	0.004	0.099	0.133	30.3	11.5	17.9
cCVDST20	208	1000	Cryogel	64	24	28	12	0.270	0.005	0.155	0.110	31.5	12.8	18.2
ST20	–	–	Initial powder	87	55	26	7	0.228	0.019	0.089	0.120	31.8	6.1	13.4
gST20	293	1	Gel	90	46	31	13	0.365	0.015	0.139	0.211	31.4	9.9	12.9
cST20	208	1000	Cryogel	89	46	30	13	0.366	0.015	0.132	0.219	33.1	10.1	13.1
gsST20	293	1	Gel/NaCl	86	40	29	16	0.415	0.013	0.136	0.267	34.9	12.0	13.5
csST20	208	1000	Cryogel/NaCl	88	43	30	15	0.402	0.014	0.146	0.242	32.7	11.1	13.2
ST63	–	–	Initial powder	84	35	41	9	0.214	0.007	0.095	0.113	32.3	8.7	10.5
gST63	298	1	Gel	69	18	36	16	0.343	0.004	0.115	0.224	34.3	14.2	12.8
cST63	208	1000	Cryogel	70	21	35	13	0.341	0.005	0.113	0.224	38.5	14.3	12.6
ST80	–	–	Initial powder	24	9	11	3	0.061	0.002	0.022	0.038	39.1	10.2	33.6
gST80	298	1	Gel	24	7	10	7	0.122	0.001	0.025	0.096	44.9	16.9	33.6
cST80	208	1000	Cryogel	24	5	12	6	0.106	0.001	0.021	0.084	43.5	15.5	33.6
ST94	–	–	Initial powder	30	14	12	4	0.100	0.003	0.034	0.062	36.8	10.1	25.1
gST94	298	1	Gel	25	7	11	7	0.151	0.002	0.041	0.108	38.5	16.7	30.1
cST94	208	1000	Cryogel	26	7	12	6	0.139	0.002	0.047	0.090	36.4	15.6	28.9

Note. Gelation of all samples was during 12 h. The first symbols in labels of dried samples correspond to cryogel (c), cryogel with 0.1 M NaCl (cs), gelation at room temperature (g) with NaCl (gs); a is the average radius of NPNP estimated from the S_{BET} value

the particulate morphology (Figs. 1–5) and crystallinity (Figs. 6 and 7) of nanoparticles. The MCA and HPC treatment effects more strongly appear (up to destroying of AST1 nanoparticles during HPC) for CFMO composed of both simple (smaller) and core-shell (larger up to 100–200 nm in size) nanoparticles. Note that each type of simple, binary, and ternary nanooxides has some specific morphological, structural, and textural characteristics [16, 17].

Nanosilica A–300, always composed of amorphous NPNP (Figs. 1, 2, and 6), is characterized by relatively stable nano-particulate morphology upon different treatments of dry and wetted powders or aqueous suspensions (Tables 1 and 2 *a*). However, supra-NPNP structures are unstable upon any treatment, and their changes depend on a type and time of the treatments in different media. The main tendency is compaction of the secondary and ternary structures with increasing time or force of a treatment (Figs. 8–11, Tables 1 and 2, S, V, $\langle R \rangle$). Pressing and stirring, *e.g.*, MCA of dry powders or HPC of frozen concentrated suspensions of A–300 at *ca*. 1000 atm, results in minimal diminution of the specific surface area (Table 1, S_{BET}). However, the pore volume, V_p (determined from the nitrogen adsorption) increases due to compaction of supra-NPNP (see $\langle R \rangle$ values, Tables 1 and 2) and increasing bulk density (ρ_b) by an order of magnitude (Fig. 10 *c*) [16, 17]. This is an apparent contradiction because it is due to more effective adsorption of nitrogen (at 77.4 K), which weakly adsorbs in broad macropores [58, 64]. Thus, small changes in the S_{BET} value are observed upon MCA of dry or weakly wetted A–300; however, there is some threshold ($h_t \approx 1.5$ g/g) of the degree of hydration of fumed silica. If $h \geq h_t$ that stronger changes are observed in the textural characteristics during relatively short time of stirring of wetted A–300 (Fig. 9, Tables 1 and 2) [26, 65].

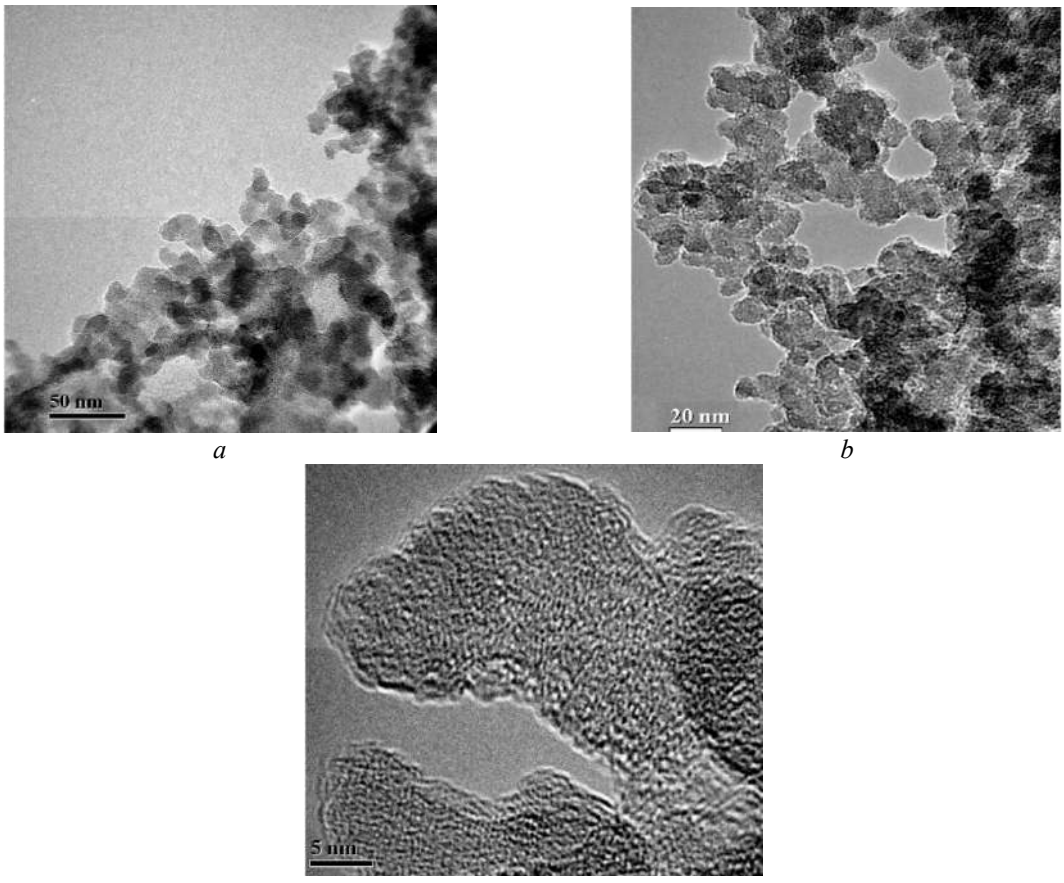

a *b*

c

Fig. 1. HRTEM images of initial A–300 of different magnification (scale bar: (*a*) 50 nm, (*b*) 20 nm, and (*c*) 5 nm)

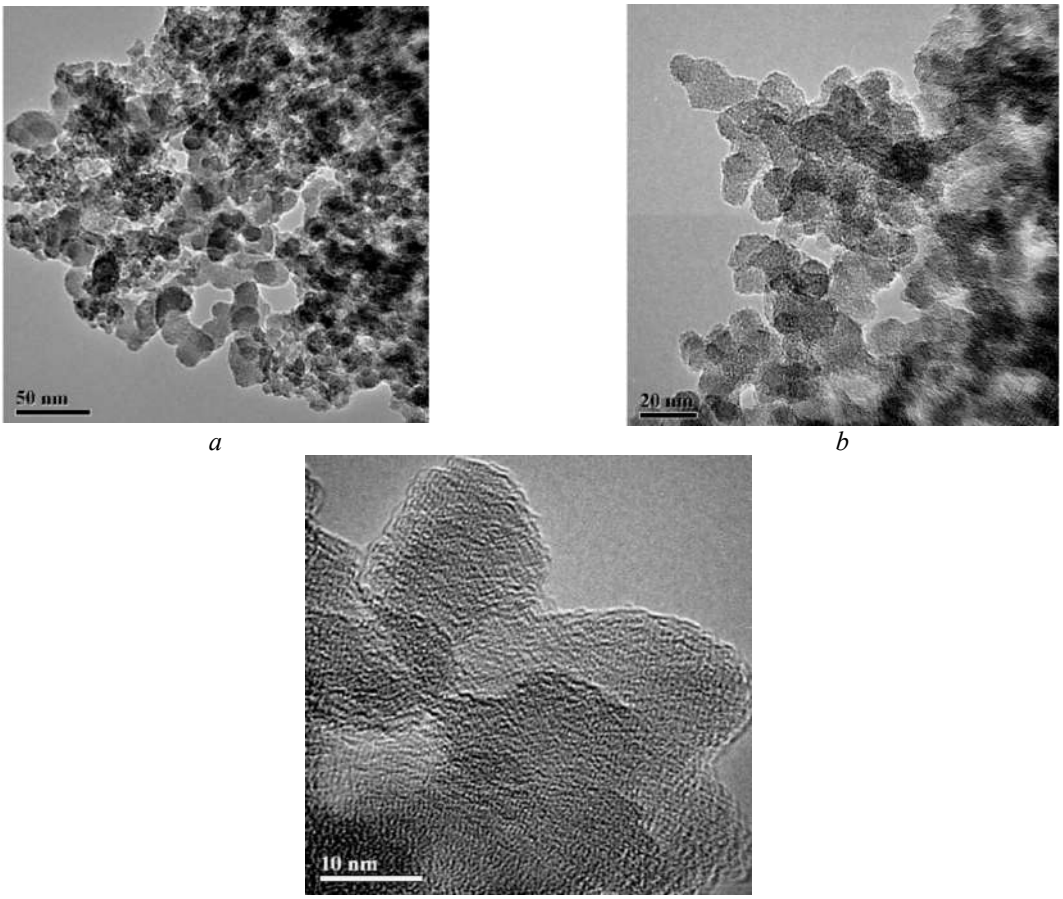

a *b* *c*

Fig. 2. HRTEM images of dried A–300 cryogel of different magnification (scale bar: (*a*) 50 nm, (*b*) 20 nm, and (*c*) 10 nm)

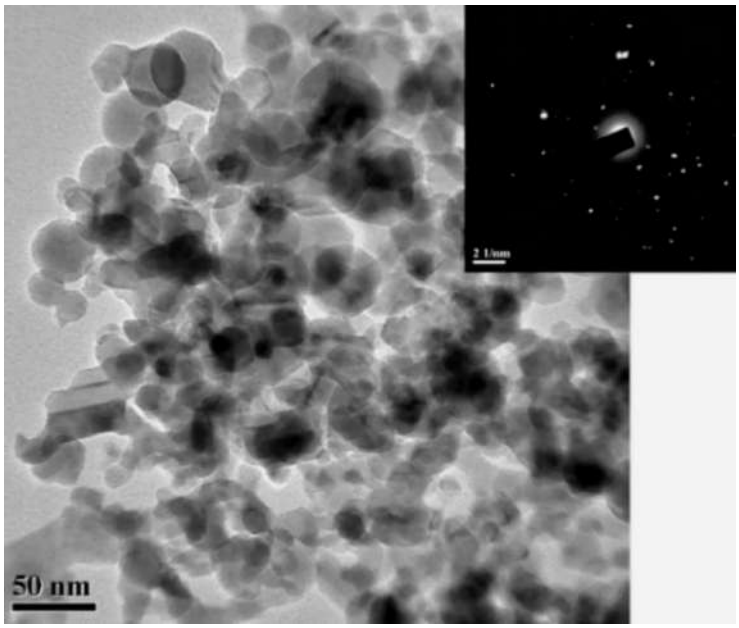

Fig. 3. HRTEM image of fumed alumina and electron diffraction pattern (insert) (scale bar 50 nm)

It should be noted that not only the amounts of a liquid but also its type affects the MCA results (Fig. 10 *c*), *e.g.*, the effects of alcohol [65] or hydrophobic solvents [16, 17] on the reorganization of supra-NPNP are smaller than that of water. This is due to several factors: (i) high polarity of water molecules and participation of all atoms in the formation of strong hydrogen bonds in contrast to alcohol or alkane molecules; (ii) small molecular size of water; (iii) penetration of the water molecules into narrower voids between adjacent NPNP and breakage of bonds (electrostatic non-valence or siloxane bridges) between these NPNP (alcohol or alkane molecules cannot do that); and (iv) clustered adsorption of water resulting in delay of the formation of a continuous hydration shell of NPNP (that is a reason of a wetting threshold at h_t). The h_t value is determined by the appearance of a continuous water phase that results in complete wetting of all NPNP (non-clustered one as at smaller h values) and compaction of wetted supra-NPNP structures to reduce the Gibbs free energy of the system [16,17]. If wetting and external action occurs without stirring (*e.g.*, HPC) or at $h < h_t$ that the reorganization of supra-NPNP is smaller than that after stirring at $h > h_t$ (Fig. 9, Table 1).

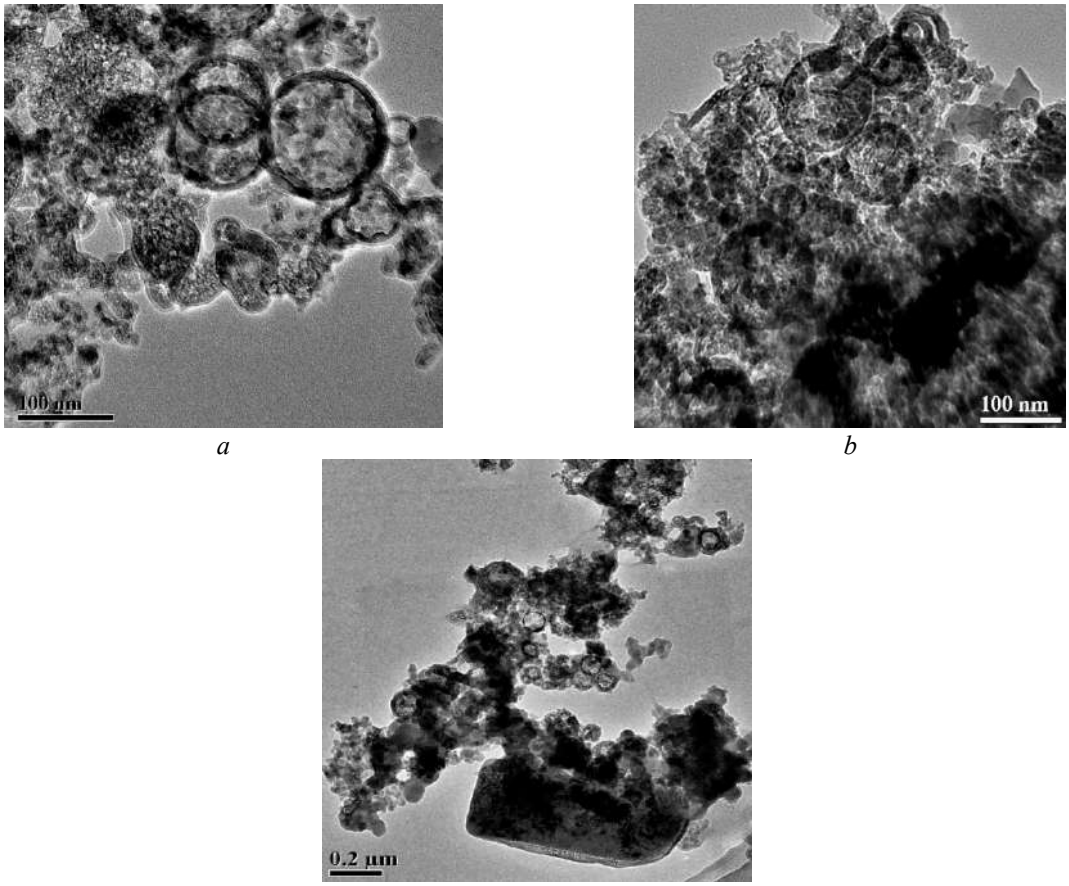

a *b* *c*

Fig. 4. HRTEM images of AST1: (*a*) initial, (*b*) dried cryogel, and (*c*) dried cryogel with NaCl (scale bar: (*a*, *b*) 100 nm, (*c*) 200 nm)

Certain compaction of A–300 supra-NPNP (NPNP aggregates) after HPC is observed in HRTEM images (Figs. 1 and 2) also demonstrating that NPNP are amorphous and spherical-like (but nonideal ones). This rough shape of NPNP causes relatively large errors of the CV/SCR model (Table 1, Δw) for initial nanosilica. These errors decrease due enhanced mechanical pretreatment of samples and an increase in contribution of the cylindrical pores due to compaction of the supra-NPNP structures and diminution of contribution of nanopores (nanovoids) with the topology poorly described by the CV model of pores. The PSD of treated

nanosilica become more uniform with a maximum intensive peak of mesopores (Figs. 8–10). Changes in conditions of gelation of A–300 result in smaller changes in the PSD in comparison to the HPC effects (Fig. 8). However, for CFMO having broader PaSD than nanosilica A–300 [16, 17, 22], the PSD of treated samples are broader (Figs. 8–13) because it is more difficult to reorganize less uniform NPNP, especially large ones, into the texture similar to that of treated A–300 composed of much smaller NPNP. Therefore, contribution of macropores increases for treated CFMO or their blends with A–300 (Tables 1–4, *S*, *V*, <*R*>). Note that some treatments (*e.g.*, MCA of dry or weakly wetted samples at h = 0.5 g/g) of A–300 alone result in enhanced macroporosity (Table 1, Figs. 8–10). MCA during different time upon treatment of dry A–300 powder and MCA of differently wetted A–300 leads to different changes in the PSD (Fig. 9). The MCA of dry A–300 gives smoother changes in the PSD *vs*. t_{MCA} (Fig. 9 *a*, *b*) in comparison to the MCA of differently wetted A–300 (Fig. 9 *c*, *d*) because strong hydro-compaction of the supra-NPNP structures occurs at $h \geq h_t$ = 1.5 g/g.

The full XRD profile analysis (FPA) applied with a self-consistent regularization procedure (using a spherical model of crystallites) without corrections on the instrumental line profile due to equipment effects provided appropriate fitting of total XRD patterns of CFMO as it was described in detail previously [66].

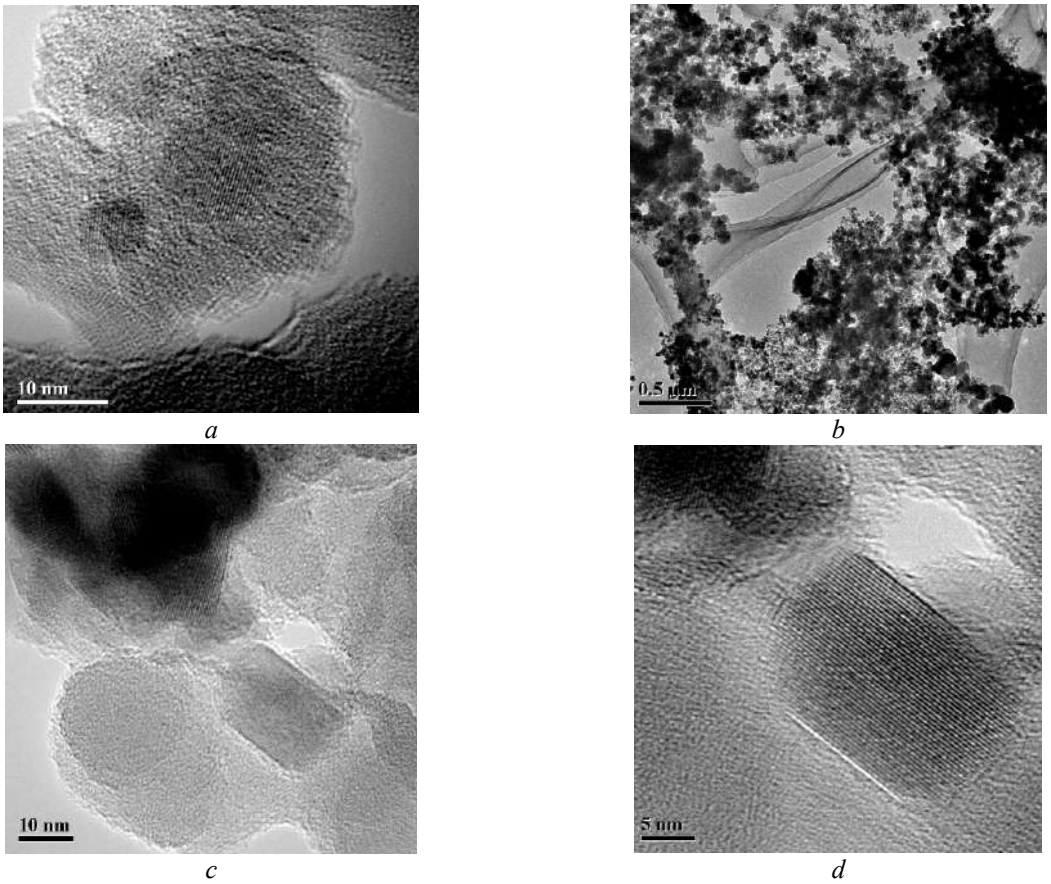

a *b* *c* *d*

Fig. 5. HRTEM images of initial (*a*) ST20 (scale bar 10 nm) and (*b-d*) ST63 at different magnifications at scale bar of (*b*) 500, (*c*) 10, and (*d*) 5 nm

In this approach, the crystallite size distributions (CSD) typically give smaller sizes of crystallites than particles observed in HRTEM images due to complex (*e.g.*, core-shell) structure of CFMO nanoparticles. The broader the XRD line (Figs. 6 and 7), the smaller is the corresponding crystallite size (Figs. 3–5) [66]. The CSD functions were also computed using the main XRD lines of crystalline titania: anatase ($2\theta \approx 25.3°$) and rutile (27.4°), and crystalline

alumina (67.1°) with consideration of an instrumental line profile due to equipment effects [66]. An increase in titania amounts in ST and AST1 results in an increase in sizes of titania crystallites (the corresponding XRD lines become narrower) because growing of titania particles (cores in core-shell particles or individual ones, Fig. 4) is faster in the flame than silica particles (shells). In the case of fumed ST20 and titania (20 wt. %) chemical-vapor deposited (CVD) onto nanosilica (CVD-ST20), the CSD functions are similar due to the same amounts of titania and the same second (silica) phase [66]. Minimum sizes of crystallites are observed for alumina alone or SA and AST1 samples. The FPA/CDS/SCR computation results are in agreement with HRTEM images (Figs. 3–5) showing the formation of crystallites in core-shall or individual NPNP [66]. According to HRTEM images of CFMO (Figs. 3–5), a surface layer of crystalline particles is always amorphous. Therefore, upon MCA, gelation, HPC, *etc*., a role of crystalline structure of NPNP cores could be minimal if the destroy of NPNP does not occur.

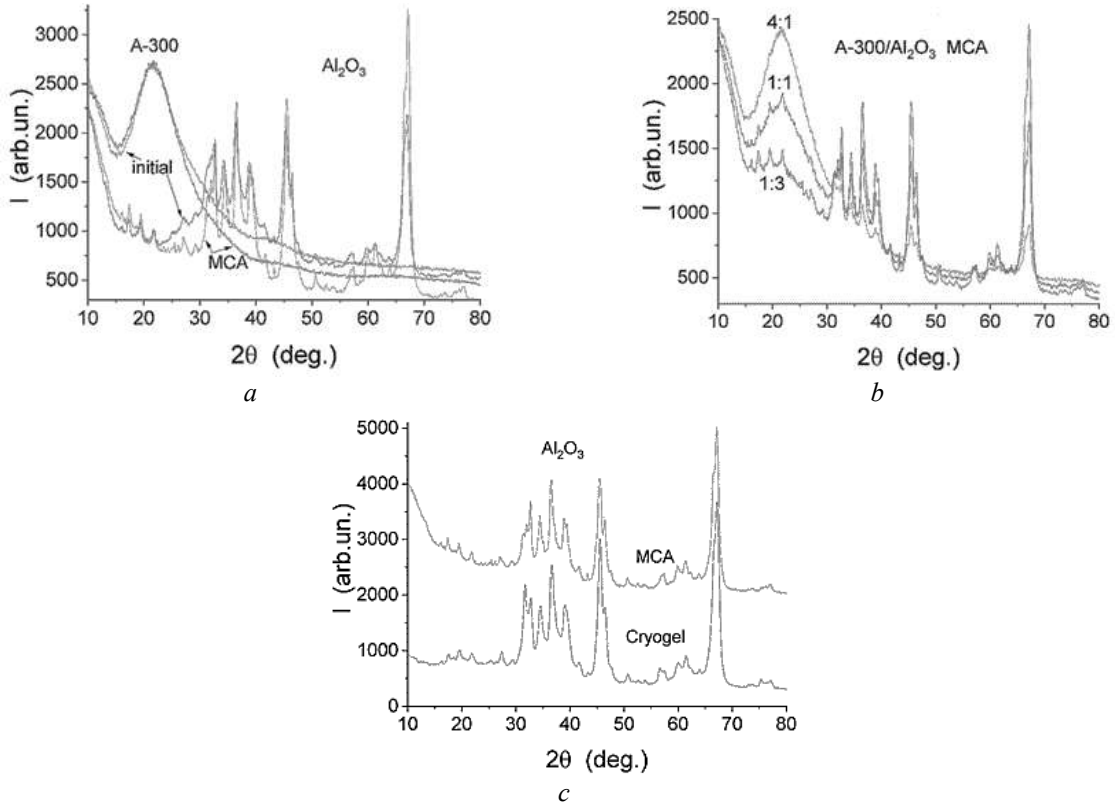

Fig. 6. XRD patterns: (*a*) initial and MCA A–300 and nanoalumina, (*b*) MCA blends of A–300/nanoalumina (4:1, 1:1, 1:3), and (*c*) nanoalumina after MCA and HPC

MCA of the dry alumina powder can enhance the crystallization, and contribution of an amorphous phase decreases (Fig. 6 *a*). A similar effect is observed upon HPC of alumina (Fig. 6 *c*) or AST1 with 89 wt. % of alumina (Fig. 7). However, addition of A–300 to nanoalumina and MCA of the dry A–300/Al_2O_3 blends diminishes this effect (Fig. 6 *b*). A similar damping effect of A–300 is observed upon different treatments of the blends with CFMO composed of larger NPNP than silica alone (Table 3, Figs. 11 and 12). For example, decomposition of large core-shell AST1 particles is not observed upon HPC of its blend with A–300 (1:1), and the S_{BET} values of samples after gelation and HPC with aqueous media or with addition of 0.1 M NaCl are similar (Table 3), in contrast to HPC of AST1 alone. The damping effect of NaCl crystallites on the breakage of the core-shell AST1 nanoparticles upon HPC is weaker than that of A–300 (Table 3, Figs. 4, 7, and 12). Additionally, NaCl (forming relatively large particles, Fig. 4 *c*) diminishes the crystallization of AST1 upon HPC in comparison to the effect observed for AST1 alone (Fig. 7 *a*).

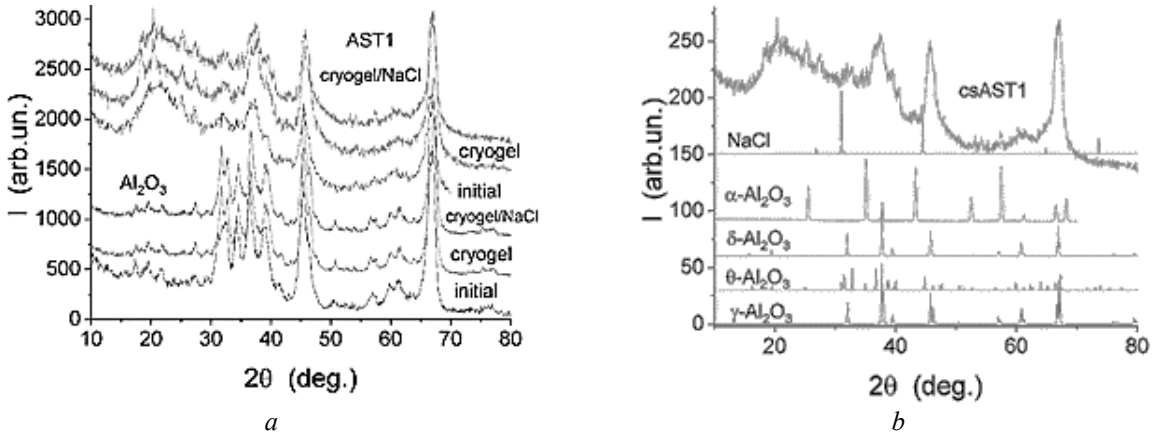

a *b*

Fig. 7. XRD patterns: (*a*) initial, cryogel (HPC), and cryogel/NaCl (HPC) of AST1 and alumina, and (*b*) csAST1 (HPC) and patterns of various crystalline alumina samples and NaCl

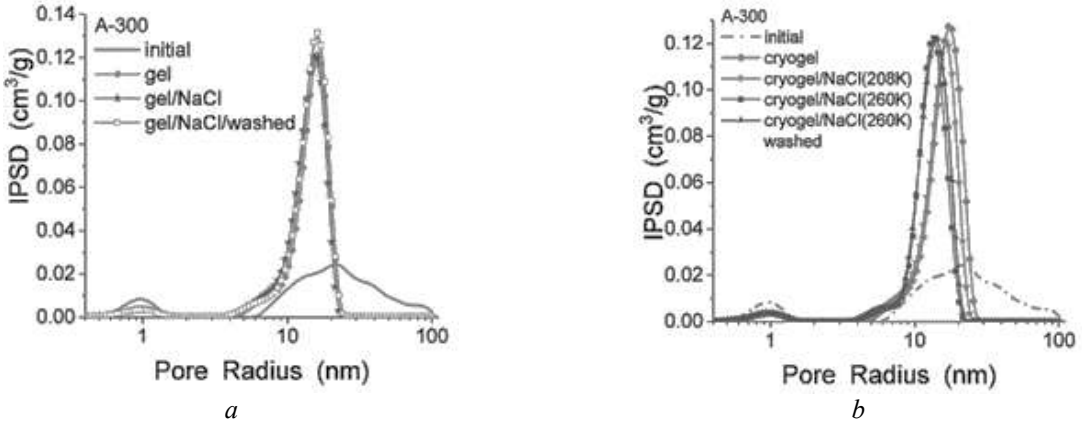

a *b*

Fig. 8. Incremental PSD (DFT CV/SCR) of degassed A–300 initial powders and dried and degassed (*a*) gels and (*b*) cryogels (HPC) differently prepared

An increase in the bulk density of MCA A–300 with treatment time (Fig. 10 *c*) leads to the displacement of the PSD peak toward smaller pore sizes (Fig. 10 *a*, *b*). This effect is general for fumed oxides [16, 17] due to features of the organization of supra-NPNP structures. However, it becomes smaller for CFMO with larger sizes of NPNP and broader PaSD due to some hindering of the reorganization of larger NPNP in the supra-NPNP structures. However, the presence of a fraction of very small NPNP, *e.g.*, in AST1 (Fig. 4), provides stronger reorganization (Fig. 12) than that for ST samples (Fig. 13) composed of larger NPNP (Fig. 5). A decrease in the S_{BET} value (*i.e.*, increase in the size of NPNP, Table 4 *a*) leads to a tendency of the displacement of the PSD peak toward large pore sizes both for gels and cryogels dried (Fig. 13). It is maximal for ST80 possessing the smallest S_{BET} value and large NPNP (Tables 1–4).

Unusual results are observed for A–300/nanoalumina samples after gelation or cryogelation (Fig. 11) because addition of A–300 composed of small NPNP (Figs. 1 and 2, Tables 1 and 2) results in broadening of the PSD. This result could be explained by opposite charging of a surface of silica (isoelectric point (IEP) is ca. 2.2, surface charges are negative in native aqueous suspensions, typically, pH 4.5–5.5) and alumina (IEP at 9.9, *i.e.*, it has positive charges at a surface of NPNP) in the aqueous media [67]. Therefore, NPNP of silica and alumina can be strongly binding in the aqueous suspensions and these bonds (of the electrostatic origin) remains after drying of the suspensions (after gelation or cryogelation).

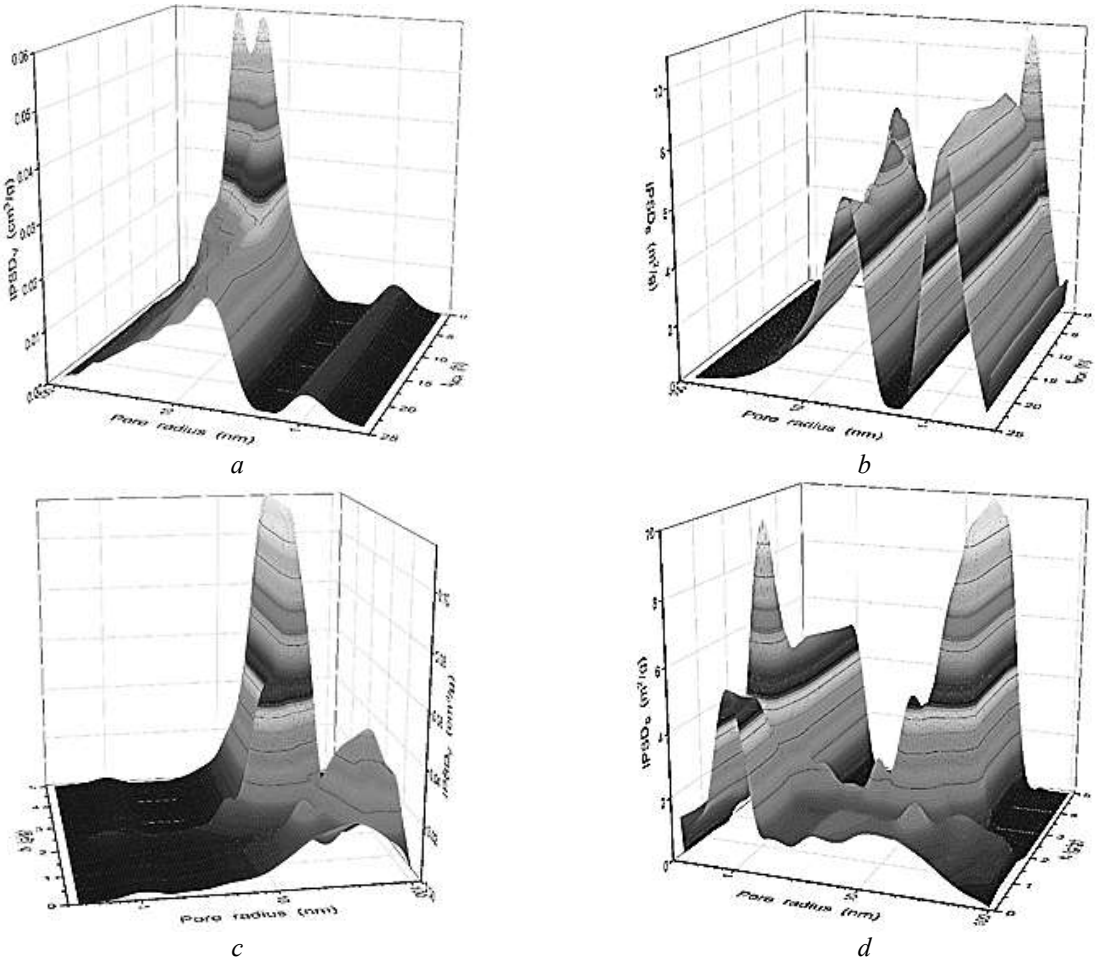

Fig. 9. Pore size distributions with respect to (*a, c*) pore volume and (*b, d*) specific surface area for A–300 after (*a, b*) MCA of dry powder *vs.* time of MCA treatment (t_{MCA}) and (*c, d*) MCA of wetted powder *vs.* the water content (*h*) (DFT VC/SCR)

In the case of AST1, NPNP surface is complex and the surface composition of CFMO NPNP determines the acid/basic properties varied due to the presence of various active surface sites. Concentrations and types of different hydroxyls such as terminal ≡MOH and bridging ≡MO(H)M≡ or $(\equiv M)_3OH$ for individual oxides (with hypervalent surroundings of metal atoms such as fivefold-O (M^V) or sixfold-O (M^{VI}) coordinated Al and Ti) and $\equiv M_1O(H)M_2\equiv$ (where M, M_1, M_2 are metal atoms) as well as other hydroxyl structures (*e.g.*, twin $M(OH)_2$) influence the behavior of complex oxides in aqueous media. Incompletely O-coordinated surface metal atoms (*e.g.*, M^{III}) correspond to the Lewis acid sites (electron-donor ones). The surface oxygen atoms with great electron density correspond to the Lewis basic sites. Bridging hydroxyls correspond to the Brønsted (B) acid sites (proton-donor ones). Typically, $\equiv M_1O(H)M_2\equiv$, *e.g.*, M_1 = Si and M_2 = Al, possesses higher B acidity than ≡MO(H)M≡ (M = Al, Ti, *etc.*). Terminal hydroxyls can be amphoteric (for silica, titania, *etc.*), *i.e.*, proton-donor or proton acceptor ones depending on the kind of an adsorbate, or basic sites (on alumina, magnesia, *etc.*), *i.e.*, electron-donor sites. Therefore, interactions of AST1 and A–300 NPNP could be weaker in the aqueous media than that for silica and alumina. This provides more effective reorganization of the AST1/A–300 supra-NPNP structures (Fig. 12) than that for A–300/alumina (Fig. 11) upon various treatments of the blends.

A type and time of treatment of FMO individual or blends more strongly affects the PSD than that of changes in the blend

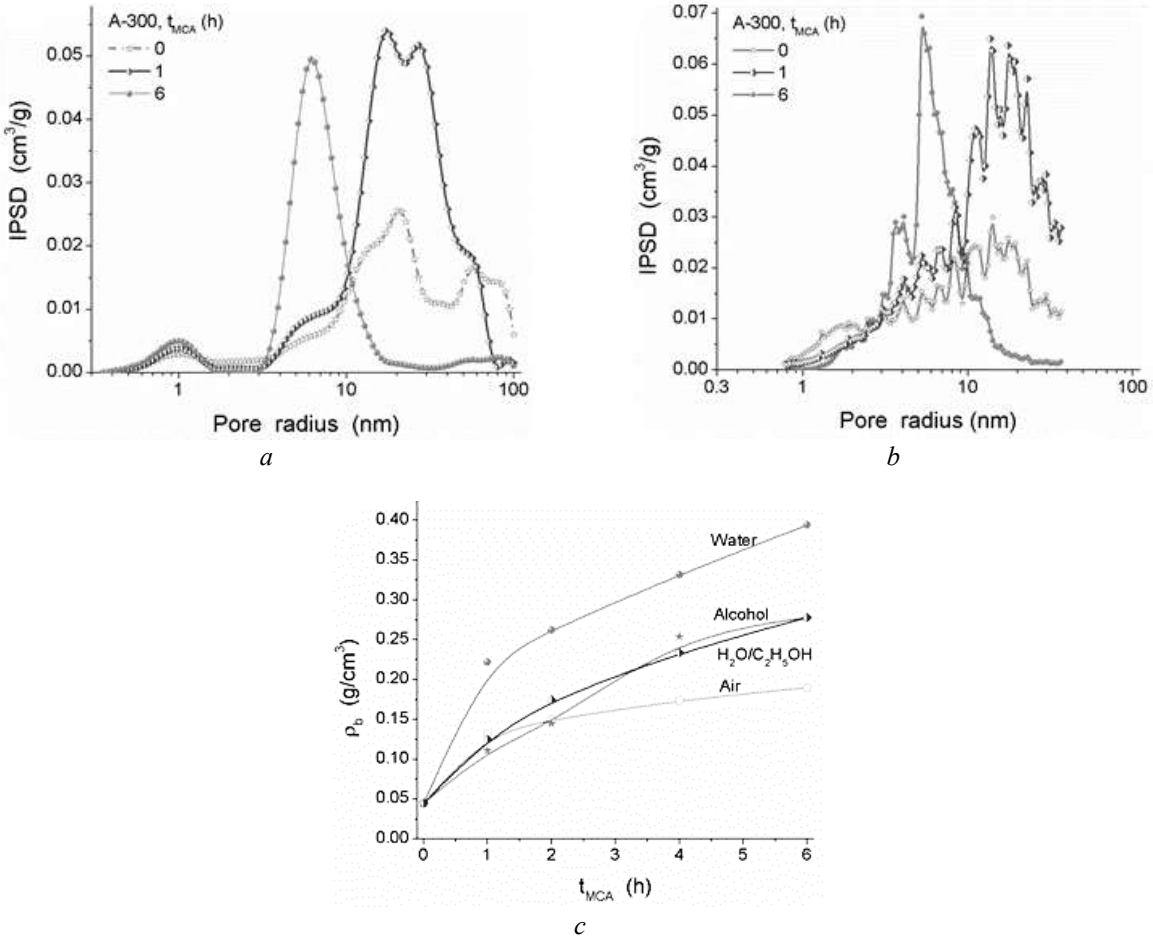

Fig. 10. Pore size distributions for A–300 initial and after MCA of wetted (h = 0.5 g/g) powder *vs.* time of MCA treatment (t_{MCA}) calculated with the DFT method using models: (*a*) CV/SCR (contributions of voids and cylindrical pores (in silica) V:C = 0.4/0.6, 0.15/0.85, and 0.1/0.9 at t_{MCA} = 0, 1, and 6 h, respectively, determined with the SCR procedure) and (*b*) NLDFT (model of cylindrical pores in silica); and (*c*) bulk density *vs.* t_{MCA} for A–300 treated in air or with addition 0.5 g of liquid (water, alcohol, or H_2O/C_2H_5OH = 1 vol/1 vol) per gram of silica

compositions (Figs. 8–13). The latter could provide practically additive results (Fig. 11). This difference could be explained by stronger changes in the supra-NPNP structures upon MCA or hydro-compaction than in the NPNP morphology even under HPC (with exception of AST1 with breakage of large core-shell NPNP under HPC). As a whole, according to the particulate (Figs. 1–7) and textural (Tables 1–4, Figs. 8–13) characteristics, all FMO keep their particulate morphology and remain texturally meso/macroporous independent of the type and time of treatments of dry or wetted powders of suspensions dried. This aspect is of importance because any studied treatment could not lead to significant losses of the morphological and textural characteristics important from a practical point of view. However, strong MCA, HPC, and hydro-compaction of FMO could lead to a certain diminution of the adsorption of high-molecular weight compounds (polymers, proteins, *etc*.) due to enhanced aggregation and narrowing of voids between NPNP. Additionally, compacted FMO with more stable supra-NPNP structures could be worse fillers of polymers. It should be noted that compaction of FMO could occur during long-term storage (several years) of the powders resulting in significant loss of the specific surface area [17, 60, 68].

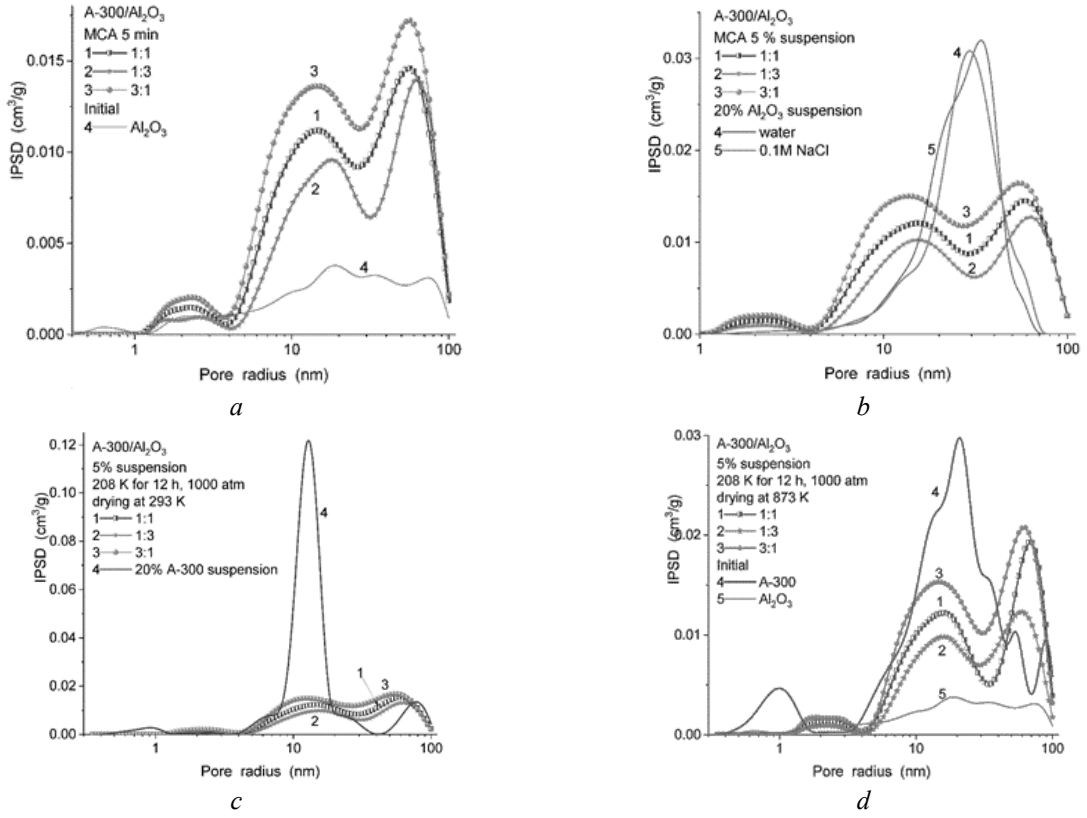

Fig. 11. IPSD of initial powders and dried and degassed A–300/nanoalumina (weight ratio 1:1, 1:3, and 3:1) blends as (*a*) powders, (*b*) dried gels, and (*c, d*) dried cryogels (HPC) differently prepared (DFT VCV/SCR)

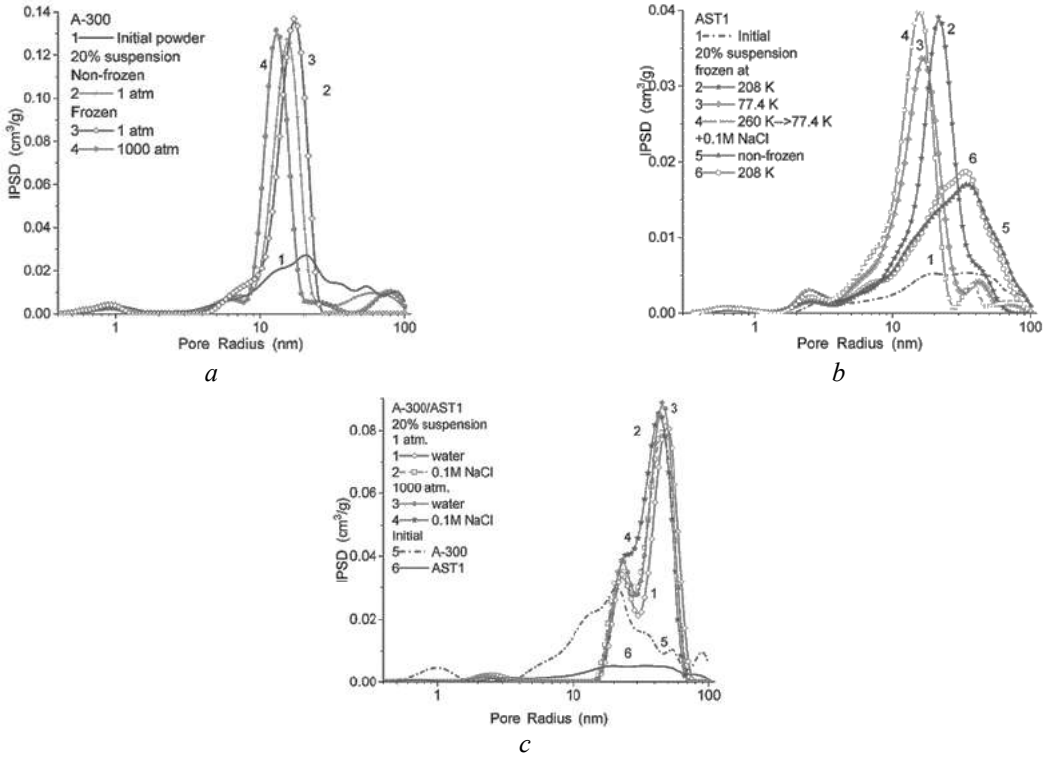

Fig. 12. IPSD of dried and degassed A–300 and AST1 powders (initial), gels, and cryogels (HPC) (*a, b*) individual and (*c*) their blend (weight ratio 1:1) differently prepared (DFT VCV/SCR)

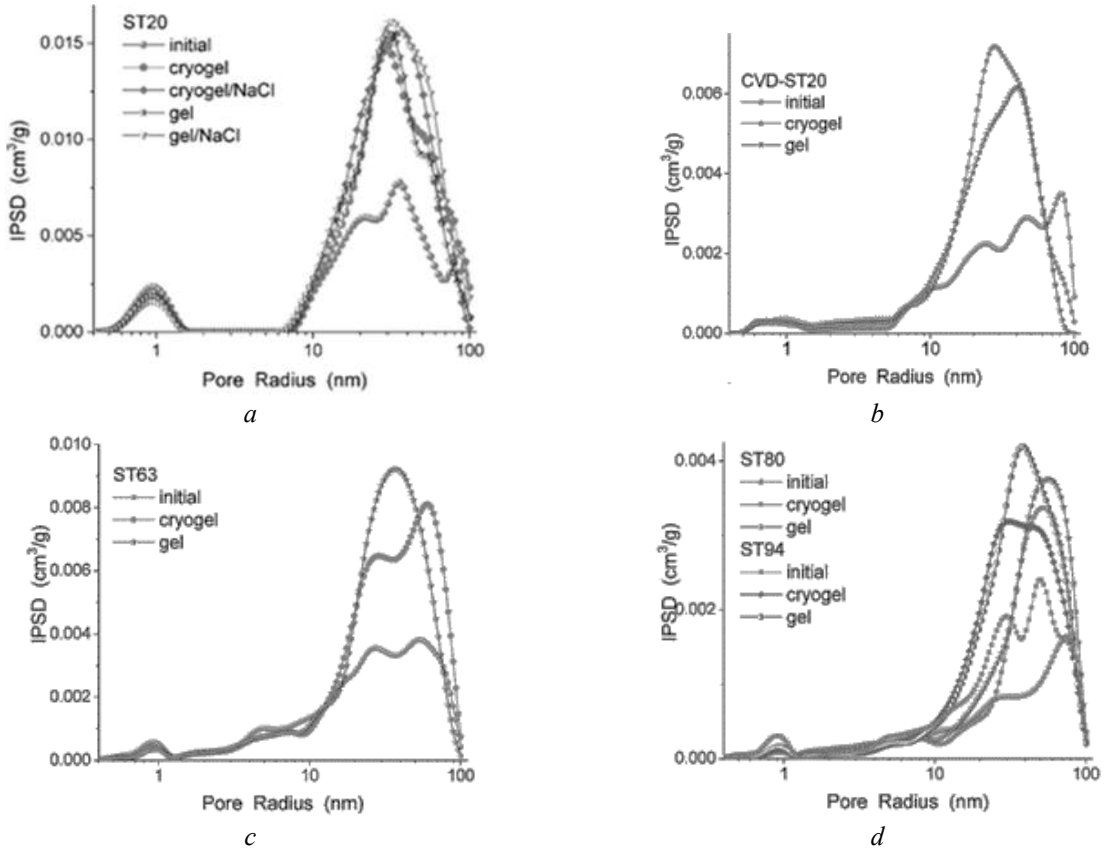

Fig. 13. IPSD of dried and degassed powders, gels, and cryogels (HPC) of silica/titania samples: (*a*) ST20, (*b*) CVD–ST20, (*c*) ST63, and (*d*) ST80 and ST94 differently prepared (DFT VCV/SCR)

CONCLUSION

According to HRTEM, XRD, and adsorption data, the characteristics and properties of fumed simple, binary, and ternary oxides depend strongly on various external actions. Gelation or high-pressure cryogelation of aqueous media pure or with certain salinity (0.1 M NaCl), and mechanochemical activation of dry or wetted powders of individual (silica, alumina, their mechanical blends) and complex (silica/titania, alumina/silica/titania, AST1, AST1/A–300) nanooxides strongly influence the particulate morphology (weaker) and textural characteristics (stronger) of treated samples. The temperature–pressure behavior of different phases (silica, alumina, and titania) under HPC leads to destroy of complex core-shell nanoparticles (100–200 nm in size) in contrast to small nonporous nanoparticles (5–20 nm). The textural characteristics of nanooxides are sensitive to any external actions due to compaction of such supra-NPNP structures as aggregates of nanoparticles, agglomerates of aggregates, and visible particles in the powders. The compaction of supra-NPNP enhances the pore volume (for adsorption of low-molecular weight compounds such as nitrogen, water, *etc*.), but it much weakly affects the specific surface area (with one exception of AST1 destroyed under HPC) because small NPNP are relatively stable during any external actions (HPC, MCA) studied. The compacted FMO materials are characterized by enhanced mesoporosity shifted to macroporosity with decreasing specific surface area and increasing sizes of nanoparticles or to mesopores with increasing MCA time or amounts of water in wetted powders treated and dried. At low hydration degree of the A–300 powder (h = 0.5 g/g), the value of S_{BET} slightly increases if MCA is provided by stirring or ball-milling (due to partial decomposition of aggregates of NPNP), but subsequent treatment results in diminution of the specific surface area (due to compaction of supra-NPNP structures); *i.e*., the surface area accessible for probe (nitrogen) molecules decreases due to stronger compaction of supra-NPNP structures. Diminution of the

freezing temperature from 208 to 77.4 K during HPC results in enhanced compaction of aggregates and agglomerates, but this treatment does not practically affect the morphology of the primary nanoparticles. The degree of decomposition of core-shell nanoparticles of AST1 does not practically increase with decreasing freezing temperature from 208 to 77.4 K. Under HPC, decomposition of core-shell AST1 particles is inhibited by added A–300 (1:1) working as a damper located between AST1 core-shell NPNP. The effect of NaCl as a damper is much weaker than that of nanosilica because NaCl forms relatively large nanoparticles. Thus, upon the use of FMO, all aspects related storage and external actions should be considered with respect to possible changes in the particulate morphological (more stable due to stability of NPNP) and textural (less stable due to a soft character of supra-NPNP structures) characteristics of the materials.

ACKNOWLEDGEMENTS

The work was supported by the National Research Foundation of Ukraine (Support of advanced and young scientists, grant 2020.02/0057). The author thanks Dr. O.I. Oranska (Chuiko Institute of Surface Chemistry, Kyiv, Ukraine), Prof. R. Leboda, Dr. J. Skubiszewska-Zięba, and Dr. B. Charmas (Maria Curie-Sklodowska University, Lublin, Poland) for some experimental data.

Морфологічні та текстурні ефекти желювання та механохімічної активації сухих та змочених простих та складних нанооксидів

В.М. Гунько

Інститут хімії поверхні ім. О.О. Чуйка Національної академії наук України
вул. Генерала Наумова, 17, Київ, 03164, vlad_gunko@ukr.net

Характеристики та властивості пірогенних оксидів суттєво залежать від різних зовнішніх впливів, що є важливим з практичної точки зору. Тому було досліджено вплив желювання та желювання при високому тиску (ЖВТ) водних суспензій, чистих та при 0.1 M NaCl, та механохімічної активації (МХА) сухих та змочених порошків індивідуальних (кремнезем, оксид алюмінію та їхні суміші) та складних (SiO_2/TiO_2 (ST), $Al_2O_3/SiO_2/TiO_2$ (AST), AST/A-300) нанолоксидів для визначення впливу їхнього складу та морфології, а також умов приготування на зміни морфологічних та текстурних характеристик тренованих зразків. Поведінка різних фаз (SiO_2, TiO_2 та Al_2O_3) нанооксидів в залежності від температури, тиску та середовища при ЖВТ може призводити до руйнування складних наночастинок типу ядро-оболонка (розміром 100–200 нм), на відміну від малих наночастинок (5–20 нм). Текстурні характеристики нанооксидів є чутливими до будь-якого зовнішнього впливу внаслідок ущільнення супрачастинок (агрегатів наночастинок, агломератів агрегатів та видимих структур порошків. Ущільнення супрачастинок приводить до збільшення об'єму пор, що визначається за адсорбцією азоту, та деякому зменшенню питомої поверхні (за винятком AST1), оскільки малі наночастинки є стабільними за використаних умов тренування. Ущільнені нанооксиди характеризуються посиленою мезопористю зі зсувом піку розподілу пор за розміром у бік макропор при зменшенні питомої поверхні (тобто при збільшенні розмірів наночастинок) або мезопор при збільшенні часу МХА чи кількості води у змочених порошках. При малій гідратації A–300 (h = 0.5 г/г) питома поверхня навіть збільшується при МХА. Зменшення температури ЖВТ з 208 до 77.4 K призводить до посилення ущільнення супрачастинок, проте це не впливає на зміни морфології наночастинок. Це також не впливає на ефект руйнування великих AST наночастинок типу ядро-оболонка. Проте руйнування цих частинок суттєво зменшується при додаванні A–300 до AST1 (1:1), тобто малі частинки обумовлюють демпферний ефект.

***Ключові слова**: нанокремнезем, нанооксид алюмінію, кремнезем/титан, глинозем/кремнезем/титан, кріогелеляція під високим тиском, морфологічні та текстурні характеристики*

REFERENCES

1. Kriechbaum G.W., Kleinschmit P. Superfine oxide powders - flame hydrolysis and hydrothermal synthesis. *Adv. Mater.* 1989. **28**(10): 330.
2. Hastie J.W. *Materials Chemistry at High Temperatures*. V. 1. *Characterization*. V. 2. Processing and Performance. (Clifton, NJ: Humana Press, 1990).
3. *Ullmann's Encyclopedia of Industrial Chemistry*. (Weinheim: Wiley-VCH, 2008).
4. *Basic characteristics of Aerosil fumed silica* 4th ed. Tech. Bull. Fine Particles 11. (Hanau: Evonik Industries, 2014).
5. *Technical Information.* TI 1176. (Frankfurt: Degussa AG, 1996).
6. Auner N., Weis J. *Oganosilicon Chemistry VI*. (Weinheim: Wiley-VCH Verlag GmbH, 2005).
7. Bhushan B. *Encyclopedia of Nanotechnology*. (Dordrecht: Springer, 2012).
8. Afyon S., Hagemann M., Somer M., Isfort C.S. Thermal and hydrothermal stability of flame hydrolytically synthesized SiO_2/TiO_2 mixed oxides. *Solid State Sciences.* 2013. **18**: 91.
9. Albers P., Maier M., Reisinger M., Hannebauer B., Weinand R. Physical boundaries within aggregates – differences between amorphous, para-crystalline, and crystalline structures. *Cryst. Res. Technol.* 2015. **50**(11): 846.
10. Schaefer D.W., Hurd A.J. Growth and structure of combustion aerosols: fumed silica. *Aerosol Sci. Technol*. 1990. **12**(4): 876.
11. Roth P. Particle synthesis in flames. *Proc. Combust. Inst*. 2007. **31**(2): 1773.
12. Pratsinis S.E. Flame aerosol synthesis of ceramic powders. *Prog. Energy Combust. Sci*. 1998. **24**(3): 197.
13. Mueller R., Madler L., Pratsinis S.E. Nanoparticle synthesis at high production rates by flame spray pyrolysis. *Chem. Eng. Sci*. 2003. **58**(10): 1969.
14. Camenzind A., Caseri W.R., Pratsinis S.E. Flame-made nanoparticles for nanocomposites. *Nano Today*. 2010. **5**(1): 48.
15. Teoh W.Y., Lutz M. Flame spray pyrolysis: An enabling technology for nanoparticles design and fabrication. *Nanoscale.* 2010. **2**(8): 1324.
16. Gun'ko V.M., Turov V.V. Nuclear Magnetic Resonance Studies of Interfacial Phenomena. (Boca Raton: CRC Press, 2013).
17. Gun'ko V.M., Turov V.V., Zarko V.I., Goncharuk O.V., Pahklov E.M., Skubiszewska-Zięba J., Blitz J.P. Interfacial phenomena at a surface of individual and complex fumed nanooxides. *Adv. Colloid Interface Sci.* 2016. **235**: 108.
18. Brown G.E.Jr., Henrich V.E., Casey W.H., Clark D.L., Eggleston C., Felmy A., Goodman D.W., Gratzel M., Maciel G., McCarthy M.I., Nealson K.H., Sverjensky D.A., Toney M.F., Zachara J.M. Metal oxide surfaces and their interactions with aqueous solutions and microbial organisms. *Chem. Rev*. 1999. **99**(1): 77.
19. Gun'ko V.M., Mironyuk I.F., Zarko V.I., Voronin E.F., Turov V.V., Pakhlov E.M., Goncharuk E.V., Nychiporuk Yu.M., Kulik T.V., Palyanytsya B.B., Pakhovchishin S.V., Vlasova N.N., Gorbyk P.P., Mishchuk O.A., Chuiko A.A., Skubiszewska-Zięba J., Janusz W., Turov A.V., Leboda R. Morphology and surface properties of fumed silicas. *J. Colloid Interface Sci*. 2005. **289**(2): 427.
20. Gun'ko V.M., Nychiporuk Y.M., Zarko V.I., Goncharuk E.V., Mishchuk O.A., Leboda R., Skubiszewska-Zięba J., Skwarek E., Janusz W., Yurchenko G.R., Osovskii V.D., Ptushinskii Y.G., Turov V.V., Gorbyk P.P., Blitz J.P., Gude K. Relationships between surface compositions and properties of surfaces of mixed fumed oxides. *Appl. Surf. Sci.* 2007. **253**(6): 3215.
21. Gun'ko V.M., Blitz J.P., Gude K., Zarko V.I., Goncharuk E.V., Nychiporuk Y.M., Leboda R., Skubiszewska-Zięba J., Osovskii V.D., Ptushinskii Y.G., Mishchuk O.A., Pakhovchishin S.V., Gorbyk P.P. Surface structure and properties of mixed fumed oxides. *J. Colloid Interface Sci.* 2007. **314**(1): 119.
22. Gun'ko V.M., Zarko V.I., Turov V.V., Oranska O.I., Goncharuk E.V., Nychiporuk Y.M., Pakhlov E.M., Yurchenko G.R., Leboda R., Skubiszewska-Zięba J., Osovskii V.D., Ptushinskii Y.G., Derzhypolskyi A.G., Melenevsky D.A., Blitz J.P. Morphological and structural features of individual and composite nanooxides with alumina, silica, and titania in powders and aqueous suspensions. *Powder Technology*. 2009. **195**(3): 245.
23. Gun'ko V.M., Bogatyrev V.M., Borysenko M.V., Galaburda M.V., Sulim I.Y., Petrus L.V., Korduban O.M., Polshin E.V., Zaulychnyy Ya.V., Karpets M.V., Foya O.O., Myronyuk I.F., Chelyadyn V.L., Dzhura U.Ya., Leboda R., Skubiszewska-Zięba J., Blitz J.P. Morphological, structural and adsorptional features of oxide composites of different origin. *Appl. Surf. Sci.* 2010. **256**(17): 5263.
24. Gun'ko V.M., Yurchenko G.R., Turov V.V., Goncharuk E.V., Zarko V.I., Zabuga A.G., Matkovsky A.K., Leboda R., Skubiszewska-Zięba J., Janusz W., Phillips G.J., Mikhalovsky S.V. Adsorption of polar and nonpolar compounds onto complex nanooxides with silica, alumina, and titania. *J. Colloid Interface Sci.* 2010. **348**(2): 546.
25. Gun'ko V.M., Turov V.V., Pakhlov E.M., Matkovsky A.K., Krupska T.V., Kartel M.T., Charmas B. Blends of amorphous/crystalline nanoalumina and hydrophobic amorphous nanosilica. *J. Non-Cryst. Solids*. 2018. **500**: 351.
26. Gun'ko V.M., Turov V.V., Pakhlov E.M., Krupska T.V., Charmas B. Effect of water content on the characteristics of hydro-compacted nanosilica. *Appl. Surf. Sci*. 2018. **459**: 171.

27. Iler R.K. The Chemistry of Silica. Solubility, Polymerization, Colloid and Surface Properties, and Biochemistry. (Chichester: Wiley, 1979).
28. Legrand A.P. *The Surface Properties of Silicas*. (New York: Wiley, 1998).
29. Bergna H.E., Roberts W.O. *Colloidal Silica: Fundamentals and Applications*. (Boca Raton: CRC Press, 2006).
30. Chuiko A.A. *Medical Chemistry and Clinical Application of Silica*. (Kiyv: Naukova Dumka, 2003). [in Russian].
31. Gun'ko V.M., Turov V.V., Zarko V.I., Pakhlov E.M., Prykhod'ko G.P., Remez O.S., Leboda R., Skubiszewska-Zięba J., Blitz J.P. High-pressure cryogelation of nanosilica and surface properties of cryosilicas. *Colloids Surf. A*. 2013. **436**: 618.
32. Gun'ko V.M., Turov V.V., Zarko V.I., Pakhlov E.M., Matkovsky A.K., Oranska O.I., Palyanytsya B.B., Remez O.S., Nychiporuk Y.M., Ptushinskii Y.G., Leboda R., Skubiszewska-Zięba J. Cryogelation of individual and complex nanooxides under different conditions. *Colloids Surf. A*. 2014. **456**: 261.
33. Gun'ko V.M., Zarko V.I., Pakhlov E.M., Matkovsky A.K., Remez O.S., Charmas B., Skubiszewska-Zięba J. Low-temperature high-pressure cryogelation of nanooxides. *J. Sol-Gel Sci. Technol*. 2015. **74**(1): 45.
34. Gun'ko V.M., Savina I.N., Mikhalovsky S.V. Cryogels: Morphological, structural and adsorption characterization. *Adv. Colloid Interface Sci*. 2013. **187–188**: 1.
35. Mills A. The freezing bomb. *Phys. Education*. 2010. **45**(2): 153.
36. Suwanchawalit C., Patil A.J., Kumar R.K., Wongnawa S., Mann S. Fabrication of ice-templated macroporous TiO_2–chitosan scaffolds for photocatalytic applications. *J. Mater. Chem.* 2009. **19**(44): 8478.
37. Nishihara H., Mukai S.R., Fujii Y., Tago T., Masuda T., Tamon H. Preparation of monolithic SiO_2–Al_2O_3 cryogels with inter-connected macropores through ice templating. *J. Mater. Chem.* 2006. **16**(31): 3231.
38. Nishihara H., Iwamura S., Kyotani T. Synthesis of silica-based porous monoliths with straight nanochannels using an ice-rod nanoarray as a template. *J. Mater. Chem*. 20008. **18**(31): 3662.
39. Gu L., Zhang J., Li L., Du Z., Cai Q., Yang X. Hydroxyapatite nanowire composited gelatin cryogel with improved mechanical properties and cell migration for bone regeneration. *Biomed. Mater*. 2019. **14**(4): 045001.
40. Nishihara H., Mukai S.R., Shichi S., Tamon H. Preparation of titania–silica cryogels with controlled shapes and photocatalysis through unidirectional freezing. *Mater. Lett*. 2010. **64**(8): 959.
41. Xu R., Yan Xu Y. *Modern Inorganic Synthetic Chemistry*. (Elsevier: Amsterdam, 2017).
42. Klotz M., Amirouche I., Guizard C., Viazzi C., Deville S. Ice templating-an alternative technology to produce micromonoliths. *Adv. Eng. Mater.* 2012. **14**(12): 1123.
43. Deville S. Freeze-casting of porous ceramics: a review of current achievements and issues. *Adv. Eng. Mater.* 2008. **10**(3): 155.
44. Niu T., Shen L. M., Liu Y. Preparation of meso-macroporous α-alumina using carbon nanotube as the template for the mesopore and their application to the preferential oxidation of CO in H_2-rich gases. *J Porous Mater*. 2013. **20**: 789.
45. Türkmen D., Bakhshpour M., Akgönüllü S., Süleyman Aşır S, Denizli A. Heavy metal ions removal from wastewater using cryogels: A review. *Front. Sustainability*. 2022. **3**: 765592.
46. Zhang M., Li Y., Uchaker E., Candelaria S., Shen L., Wang T., Cao G. Homogenous incorporation of SnO_2 nanoparticles in carbon cryogels via the thermal decomposition of stannous sulfate and their enhanced lithium-ion intercalation properties. *Nano Energy.* 2013. **2**(5): 769.
47. Shlyakhtin O.A., Oh Y.-J. Inorganic cryogels for energy saving and conversion. *J. Electroceram.* 2009. **23**: 452.
48. Mukai S.R., Nishihara H., Shichi S., Tamon H. Preparation of porous TiO_2 cryogel fibers through unidirectional freezing of hydrogel followed by freeze-drying. *Chem. Mater*. 2004. **16**(24): 4987.
49. Pons A., Casas L.l., Estop E., Molins E., Harris K.D.M., Xu M. A new route to aerogels: Monolithic silica cryogels. *J. Non-Crystal. Solid*. 2012. **358**(3): 461.
50. Tamon H., Akatsuka T., Mori H., Sano N. Synthesis of zeolite monolith with hierarchical micro/macropores by ice-templating and steam-assisted crystallization. *Chem. Eng. Trans.* 2013. **32**: 2059.
51. Babić B., Kokunešoski M., Miljković M., Prekajski M., Matović B., Gulicovski J., Bučevac D. Synthesis and characterization of the SBA-15/carbon cryogel nanocomposites. *Ceramic. Int.* 2012. **38**: 4875.
52. Maroni F., Bruni P., Suzuki N., Aihara Y., Agostini M., Branchi M., Navarra M.A., Nobili F., Matic A., Croce F. V_2O_5 cryogel: A versatile electrode for all solid state lithium batteries. *J. Electrochem. Soc*. 2019. **166**: A3927.
53. Kim J.W., Tazumi K., Okaji R., Ohshima M. Honeycomb monolith structured silica with highly ordered, three-dimensional interconnected macroporous walls. *Chem. Mater*. 2009. **21**(15): 3476.
54. Hong C., Zhang X., Han J., Du J., Zhang W. Camphene-based freeze cast ZrO_2 foam with high compressive strength. *Mater. Chem. Phys.* 2010. **119**(3): 359.
55. Tarutani N., Hashimoto M., Ishigaki T. Organic–inorganic hybrid nanocrystal-based cryogels with size-controlled mesopores and macropores. *Langmuir.* 2021. **37**(9): 2884.
56. Sinkó K. Gel-derived porous alumina systems. *Mater. Lett*. 2013. **107**: 344.
57. Zhang H., Cooper A.I. Aligned porous structures by directional freezing. *Adv. Mater.* 2007. **19**(11): 1529.

58. Gregg S.J., Sing K.S.W. *Adsorption, Surface Area and Porosity*. 2nd ed. (London: Academic Press, 1982).
59. Gun'ko V.M. Textural characteristics of composite adsorbents analyzed with density functional theory and self-consistent regularization procedure. *Him. Fiz. Tehnol. Poverhni*. 2020. **11**(2): 163.
60. Gun'ko V.M. Morphological and textural features of various materials composed of porous or nonporous nanoparticles differently packed in secondary structures. *Appl. Surf. Sci.* 2021. **569**: 151117.
61. Gun'ko V.M., Mikhalovsky S.V. Evaluation of slitlike porosity of carbon adsorbents. *Carbon.* 2004. **42**(4): 843.
62. Neimark A.V., Ravikovitch P.I. Capillary condensation in MMS and pore structure characterization. *Microporous Mesoporous Mater.* 2001. **44**/**45**: 697.
63. *JCPDS Database*. International Center for Diffraction Data. PA, 2001.
64. Adamson A.W., Gast A.P. *Physical Chemistry of Surface*. Sixth edition. (New York: Wiley, 1997).
65. Gun'ko V.M., Voronin E.F., Nosach L.V., Turov V.V., Wang Z., Vasilenko A.P., Leboda R., Skubiszewska-Zięba J., Janusz W., Mikhalovsky S.V. Structural, textural and adsorption characteristics of nanosilica mechanochemically activated in different media. *J. Colloid Interface Sci.* 2011. **355**(2): 300.
66. Gun'ko V.M., Oranska O.I., Paientko V.V., Sulym I.Ya. Particulate morphology of nanostructured materials. *Chem. Phys. Technol. Surf.* 2020. **11**(3): 368.
67. Gun'ko V.M., Zarko V.I., Leboda R., Chibowski E. Aqueous suspensions of fumed oxides: particle size distribution and zeta potential. *Adv. Colloid Interface Sci.* 2001. **91**(1): 1.
68. Gun'ko V.M., Turov V.V., Goncharuk O.V., Pakhlov E.M., Matkovsky O.K. Interfacial phenomena at a surface of individual and complex fumed nanooxides. *Surface*. 2019. **11**: 3.

Received 16.05.2022, accepted 05.12.2022